2023

A Comparative Biomechanical Investigation of Porcine Neonatal and Adult Left Ventricular Tissues

Timothy R. Eastep

A Comparative Biomechanical Investigation of Porcine Neonatal and Adult Left Ventricular Tissues

by

Timothy Ryan Eastep

Presented to the Faculty of the Graduate School of The University of Texas at

Arlington in Partial Fulfilment

Of the Requirements for the Degree of

MASTER OF SCIENCE IN BIOMEDICAL ENGINEERING

THE UNIVERSITY OF TEXAS AT ARLINGTON

May 2023

Abstract

A Comparative Biomechanical Investigation of Porcine Neonatal and Adult Left Ventricular Tissues

Timothy Ryan Eastep, MS

University of Texas at Arlington, Bioengineering 2023

Supervising Professor: Dr. Jun Liao

A current trend in cardiac muscle regeneration and repair is to recreate the biophysical and biomechanical environment of the neonatal hearts, which has been shown to promote cardiac regeneration. This translational need requires thorough understanding of the biomechanical properties of the neonatal hearts. In this study, we aim to (i) characterize the dynamic viscoelastic properties of the neonatal porcine left ventricular (LV) muscle and compare with the adult tissue behavior using a rheometer; (ii) perform histological assessment to identify the cellular and extracellular (ECM) microstructures that contribute to the observed biomechanical differences, and (iii) develop a light sheet imaging protocol to visualize the 3D ECM networks of both the neonatal and adult LV muscles. We found that the dynamic viscoelastic properties of the neonatal porcine LV muscle tissues were drastically different from the adult LV muscle tissues. The adult LV muscle tissues had much greater storage modulus (G') and larger loss modulus

(G”) than the neonatal LV muscle tissues in the range of frequency sweep. When compared with the adult LV, the histology of neonatal LV muscle showed less organized immature heart muscle fibers, a lower amount of collagen network, and a higher amount of proteoglycans, which were likely the underlying contributors of the unique viscoelastic properties of the neonatal heart muscles. Lastly, we have developed a tissue preparation and imaging protocol that was able to capture 3D ECM fiber orientation and alignment for both the neonatal and adult heart muscles.

TABLE OF CONTENT

LIST OF FIGURES

CHAPTER 1:

1 Introduction

1.1 Myocardial Infarction (MI)

Cardiovascular diseases (CVD) are the leading cause of death in the US[1]. CVD kills approximately 877,500 Americans annually. This costs the healthcare industry $216 billion per year [2]. Among CVD, ischemic CVD occurs when a reduction of blood flow happens most commonly due to plaque buildup in the arteries. When coronary arteries were blocked, the reduction of blood flow causes downstream oxygen restriction and leads to cardiomyocyte death in the ventricular wall [3-9]. Following MI, the injured region experiences necrotic response, fibrotic response, and later ventricular wall remodeling. The pathological development can be the extension of the infarcted tissue, scar tissue formation, ventricular wall thinning and dilation, loss of cardiac function, and eventually heart failure (HF) [10-11].

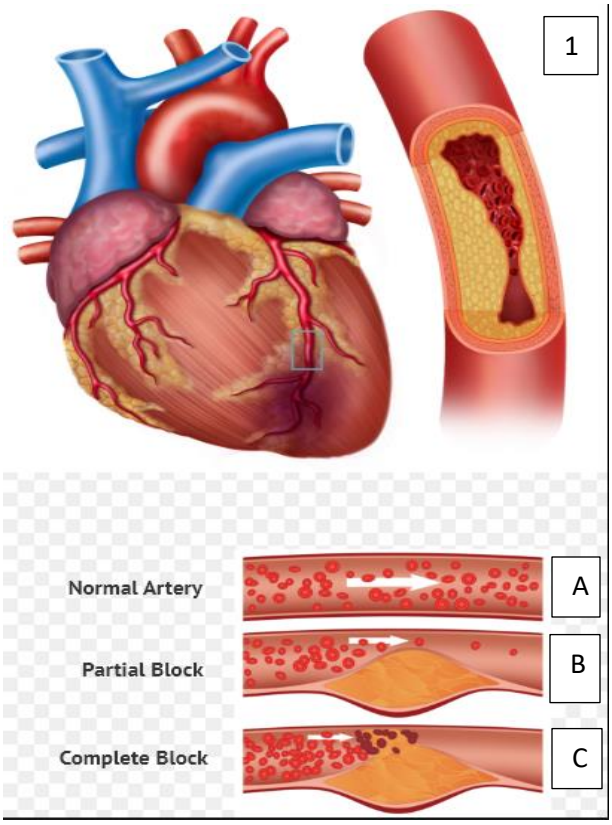

Figure 1.1: Plaque blocking artery with darkened tissue indicating necrosis. (A) Normal artery with blood flow; (B) Partial block with reduced blood flow; (C) Complete block of artery [12].

1.2 Conventional treatments for MI, Limitations, and Current Trends

Currently, diagnosis of MI is accomplished by an echocardiogram (ECG). This diagnostic tool should be administered and interpreted within ten minutes of the patient showing symptoms of MI. Continuous administration of the ECG should be administered at fifteen-to-thirty-minute intervals if the initial ECG shows proof of MI [13]. Measurement of cTn levels should be taken into consideration. Elevated cTn level is a reliable indicator of MI. Once confirmed, patients can receive conventional MI treatment options to achieve reperfusion, which include fibrinolytic therapy (FT) and primary percutaneous coronary intervention (P-PCI).

FT should be used if P-PCI is not a viable option due to the time constraint needed to administer P-PCI. This method of treatment is administered to dissolve the blood clots

accumulated during MI. FT drugs include Tenecteplase, Retaplase and Alteplase. Generally, these are administered following Aspirin or Clopidogrel. P-PCI should be used if time permits. The benefit of this treatment is that it allows for immediate opening of the blockage. This is important because the lack of blood flow from the MI causes the necrosis of the tissue. It is difficult to revascularize and revive the injured tissue after necrosis. Overall, PCI is the preferred treatment since this approach allows for relatively adequate reperfusion of the artery. In instances such as a combination of endothelial injury, atheroembolization, and edema, PCI treatment also experiences inadequate myocardial reperfusion [13].

Although these are the preferred treatment options, there are some limitations to those conventional treatments of MI. Even after FT or P-PCI, complications can arise. The patient can still experience deterioration of cardiac function and eventually progression towards heart failure (HF). For example, when using stents, the patient can experience lesions in the target location. This can lead to lowered left ventricular function, or renal insufficiency [14]. Restenosis is another common occurrence in patients who have experienced MI and followed stent treatment. For MI patients progressing towards HF, heart transplants remain the gold standard of life saving and an improved life quality. Unfortunately, the shortage of donor hearts and challenges caused by immune compatibility make this approach unavailable to the majority of HF patients.

Most importantly, all the conventional treatments are lack of capabilities to promote heart muscle regeneration. The loss of cardiomyocytes after MI are permanent due to the poor regenerative potential of heart muscles, and the fibrotic scarring further worsens the situation. It is known that the cardiomyocyte regenerative properties in the adult human heart have a turnover of 1%. This makes the adult heart unable to regenerate cardiac tissue following a MI [15]. Many current research efforts thus have been focusing on cardiac regeneration, with a goal to

repair the damaged heart muscle by triggering cardiomyocyte regeneration via delivering various stem cells, scaffolds, and/or biofactors.

1.3 Cardiac regeneration in neonatal pigs and the importance of neonatal heart microenvironment

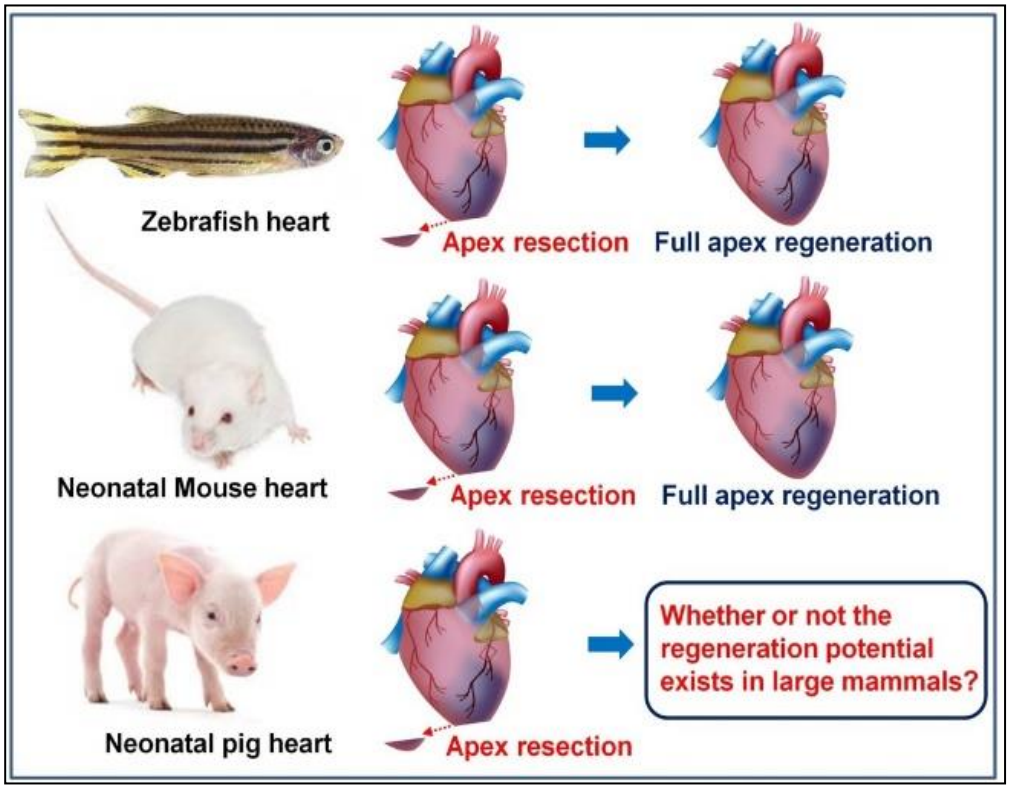

Figure 1.2: The reported full apex regeneration capability in zebrafish and mouse heart, and the research question about cardiac regenerative potential in large mammals.

Recently, a few key studies have demonstrated that cardiac regeneration could occur in zebrafish and mice after apex being resected[16,18,19,17,20-24]. Both zebra fish model and mouse model showed that full apex regeneration could be achieved in the first few days post-

birth, and the heart lost full regeneration potential after 7 days post-birth. Recently, our group conducted and published a study using a partial apex resection neonatal pig model to investigate if the observed full cardiac regenerative potential occurs in large mammals (**Figure 1.2**).[16-17] We performed partial apex resection on 0-day old (within day 1 post-birth) and 7-day old neonatal pigs and tracked the degree of apex regeneration 4 weeks after resection surgery. Our study showed that the piglets lost their full regenerative capacity 7 days post-birth, but preserve great regenerative potential within 1 day of birth. Our finding with the neonatal pig model confirmed the reported timeframe of cardiac regeneration in zebra fish and mouse models.[16-17]. The transient regeneration potential we observed in the partial apex resection neonatal pig model is also consistent with a recent study, which reported that the neonatal pig heart, during the first days of life, was capable of regeneration following acute myocardial infarction created by permanent ligation of the left descending coronary artery [13].

Two important observations in our study pointed out that the microenvironments of neonatal heart pay important roles in preserving full cardiac regenerative potential [25]. We noted that the 0-day-old heart muscle tissue was more pliable, and the partial apex resection could be more easily performed when compared with the 7-day-old hearts, which had more rigid heart muscle tissue [25]. The underlying reason for the quickly increased heart tissue stiffness and decreased tissue pliability after the piglet's birth is the rapid deposition and maturation of the collagen network, which binds the heart muscle fibers and forms the cardiomyocyte ECM lacunae [25-28]. This observation indicates that the structural and mechanical properties of the neonatal heart ECM was likely one of the factors in contributing to full cardiac regenerative potential [25]. At the injury site of the 0-day old piglet heart, we demonstrate that cells were actively dividing and differentiating towards young cardiomyocytes, further suggesting the

neonatal heart microenvironment has factors that promote heart muscle regeneration [25-26]. Thus, the biomechanical, structural, and compositional properties in the neonatal heart need to be better understood.

1.4 Proposed research & significance

Aim 1: Characterize the dynamic viscoelastic properties of the neonatal porcine left ventricular (LV) muscle and compare with the adult tissue behavior using a rheometer.

In this aim, we performed rheology testing on both neonatal and adult left ventricles. The significance of this study was to determine the dynamic viscoelastic properties of both types of LV tissues under a range of physiologically relevant frequency. The sweep frequency in rad/s was determined by converting to Hz, which can be correlated to heartbeat. The study was performed to determine the viscoelastic behavior of the neonatal heart and how it is different from adult heart, as well as at what frequency their behavior is mostly different from each other. This was accomplished by measuring the loss and storage modulus exhibited by the LV tissue at the above-mentioned frequency range.

Aim 2: Perform histological assessment to identify the cellular and extracellular (ECM) microstructures that contribute to the observed biomechanical differences.

In this aim, we performed histological study of the left ventricle samples of both neonatal and adult heart tissues. Both the circumferential sections and longitudinal sections were dissected, and Movat's Pentachrome staining was performed for light microscopic imaging. Movat's Pentachrome stained heart muscle in red, collagen in yellow, elastin in black, and

proteoglycans in blue. This method allows us to compare the microstructures of the neonatal and adult LV tissues at both longitudinal and circumferential orientations.

Aim 3: Develop a light sheet imaging protocol to visualize the 3D ECM networks of both neonatal and adult LV muscles.

In this aim, we are developing a tissue preparation and light sheet microscopy protocol for both the neonatal and adult LV tissues. This process has the potential to reveal cellular structure and extracellular matrix (ECM) structure three dimensionally in large volume. It has been shown that light sheet imaging is capable of reconstructing 3D morphology of tissues after proper tissue clearance. In this first stage, we are specifically focusing on visualizing the heart ECM.

CHAPTER 2: EXPERIMENTAL METHODS

2.1 Rheological testing

2.1.1 Instrument

Rheological testing was conducted by using a rheometer (Anton Paar modular compact rheometer (MCR) 302). By using the plate-plate configuration, we were able to measure the dynamic viscoelastic properties of a material.

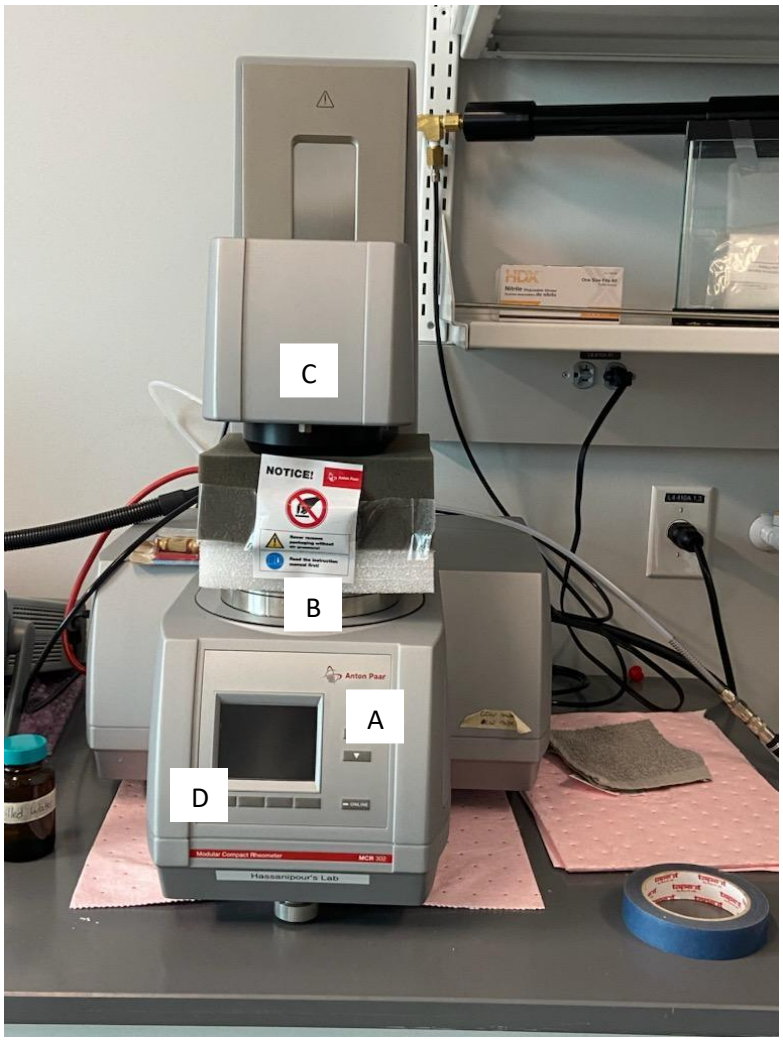

Figure 2.1: Anton Paar MCR 302. (A) MCR body; (B) Measuring plate; (C) Head; (D) Softkeys

In **Figure 2.1,** the MCR can be seen in the docked position. The docked position indicates that the head is lowered down onto a foam pad. This foam pad creates a barrier that protects the head from getting damaged from accidental movement from passersby. The instrument uses a hood that covers the measuring system. This hood prevents any debris from impacting the system. It also helps maintain specified temperature set during testing parameters.

The MCR has uses a fluid circulator. The fluid circulator allows for controlled temperature adjustments of the instrument when testing. This device is a liquid controlled

temperature system containing a filter to clean the circulating water and a color-coded indicator that indicates when it needs to be replaced.

Next, the measurement system is attached. Each system has a Toolmaster™ chip that is in the shaft of each system. This chip is pre-loaded with the geometry dimensions, safety limitations, and calibration constants for the system during use.

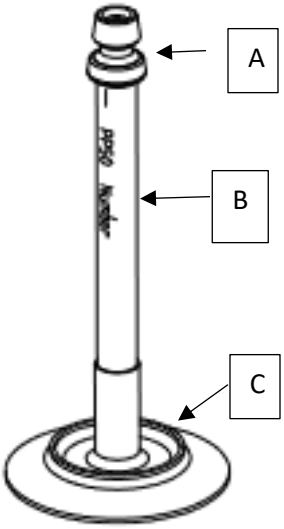

Figure 2.2: Plate-plate system geometry. (A)Toolmaster™ chip inside the shaft head; (B) Geometry shaft; (C) Specific system geometry [30].

The plate-plate system can be used for highly viscous samples. The geometry of the system makes it ideal for tissue samples that are viscoelastic. There is a larger range of shear due to the flat geometry of the plate (**Figure 2.2, 2.3**). It is easy to clean, and the temperature is easy to maintain. Due to compression along the flat surface, the sample can dry out over time and there are sometimes variations in shear along the surface of the measuring geometry.

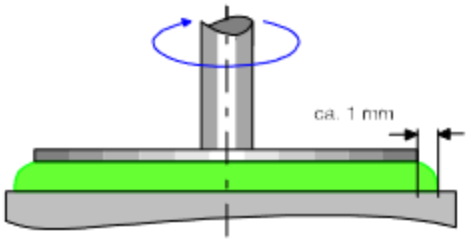

Figure 2.3: Plate-plate system [30].

2.1.2 Measurement software

The measurement software used for this research was RheoCompass^{TM}. This is a rheology software developed by Anton Paar. It has predefined testing templates in the home screen (**Figure 2.4**). After mounting the sample and lowering top plate until to reach the sample, the ready screen helps to monitor the testing status, normal force, temperature, and plate-gap.

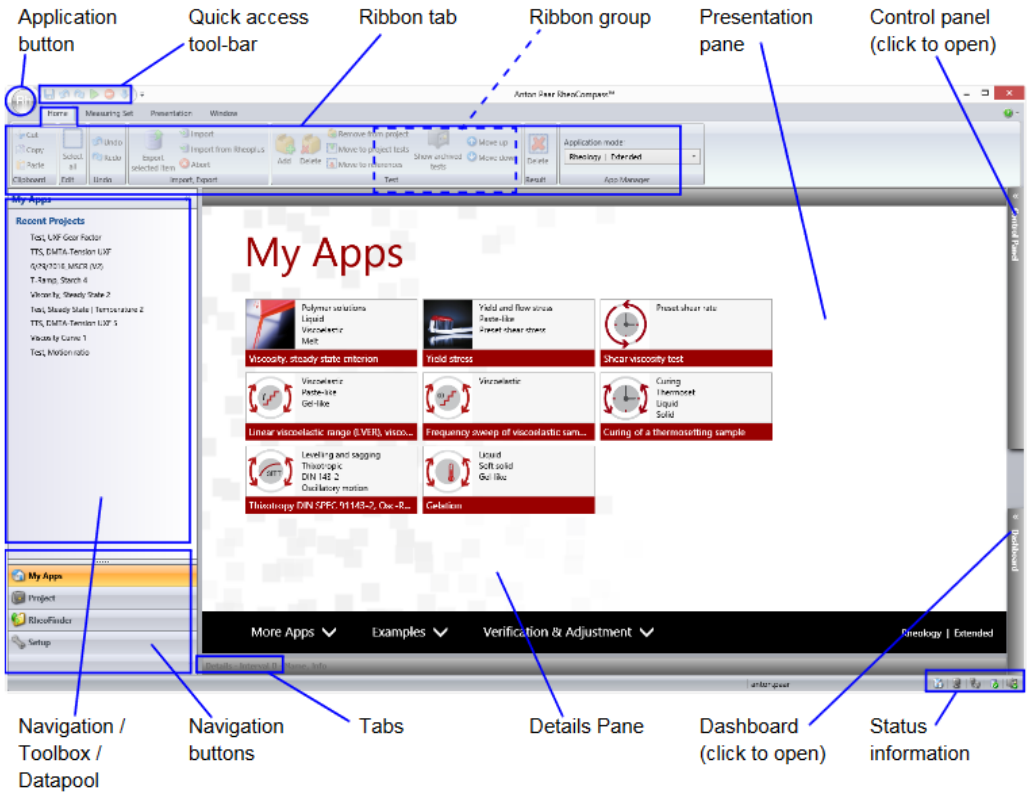

Figure 2.4: Overview of the home panel of Rheocompass^{TM}[31]

2.1.3 Testing Parameters

Our rheological study of the neonatal and adult porcine left ventricles required a plate-plate geometry. This system geometry was beneficial because we were able to prepare relatively flat samples that would fit between the geometry and the measurement plate. In our study we wanted to determine the viscoelastic properties of the LV tissue at different heart rates. To accomplish this, we needed to conduct a frequency sweep. In this study, we focused our frequency sweep on a range of 0-160 rad/s (N=3 for neonatal; N=3 for adult). This allowed us to determine the viscoelastic responses of both the neonatal and adult LV tissues in a frequency that is physiologically relevant. We set our samples to be under a constant normal force of 1-1.3 Newtons. We accomplished this by slowly lowering the plate geometry down in small increments until we were close to our target gap and the normal force was within the set parameters.

The data is recorded as a storage modulus (G') and a loss modulus (G"). The storage modulus is the amount of energy that is stored in a specific sample. When this value is higher than the loss modulus, the sample is acting more elastically due to the stored energy. The loss modulus is the opposite. The Loss modulus is the amount of energy that is expelled due to heat. When this happens, the tissue displays more viscous properties, and the loss modulus will show a higher value than the storage modulus.

2.1.4 Sample preparation

Our samples were from hearts obtained from two different locations. The adult hearts were procured from a local slaughterhouse after all necessary USDA paperwork was filled out. The neonatal pig hearts were obtained from a farm in Mississippi. The hearts were obtained from 1-day old piglets. The hearts were cold stored and shipped to our lab at the University of Texas at Arlington. The hearts were counted, labeled and frozen for future testing. This allowed for testing logistics of the rheometer.

Three of the adult hearts and three of the neonatal hearts were thawed by placing them in the refrigerator. This allowed for controlled thaw to prevent damage to the tissue. When hearts were thawed completely dissection began. The adult hearts were dissected first (**Figure 2.5**). All samples were taken from the anterior left ventricles of each heart.

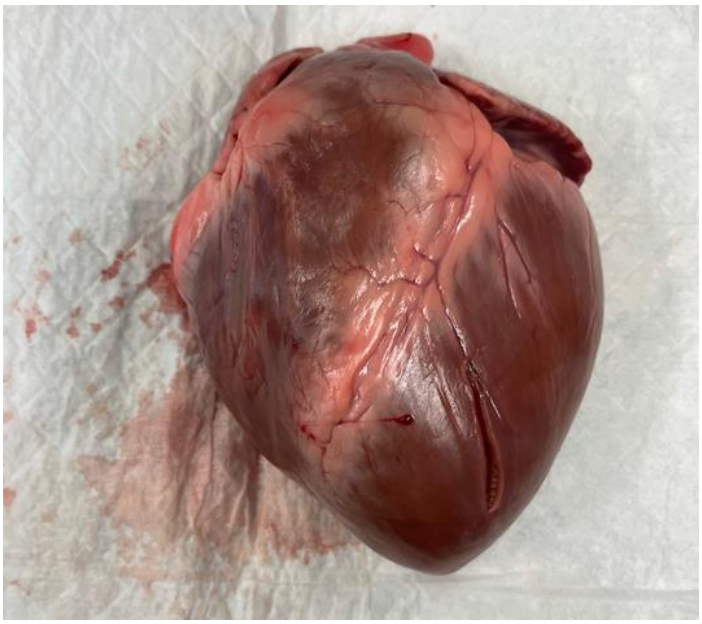

Figure 2.5: Adult porcine heart (anterior view).

The left ventricular wall of the neonatal heart was dissected to the right geometry and used as the sample for rheology testing (**Figure 2.6**). Due to the large thickness of the adult left

ventricle. The samples were stored in labeled specimen jars containing Phosphate Buffer Saline (PBS). PBS can mimic the environment of the body[32].

Figure 2.6: Neonatal porcine heart (anterior view).

2.2 Histology, light microscopy, and microstructural analysis.

2.2.1 Histology

Samples of both the longitudinal and circumferential orientations of the tissue were dissected from both the adult and the neonatal hearts. These samples were stored in glass vials. The samples were fixed in formaldehyde. Samples were then embedded in wax, sectioned into 5

μm slices, and stained with Movat's pentachrome protocol. The Movat's Pentachrome staining allows for color indication of components of the heart tissues. This staining would also allow us to color stain the different components of the heart tissue to determine the orientation and quantity. With Movat's Pentachrome staining, we were able to have heart muscle stained in red, collagen in yellow, elastin in black, and proteoglycan in blue. This would allow us to determine how the neonatal cardiac tissue differs from the adult cardiac tissue.

The histological slides were imaged under white field light using a light microscope (Eclipse Ti, Nikon). For muscle fiber orientation analysis, the histological images of the Movat's pentachrome staining were converted to 8-bit gray scale images using Orientation J plugin in Image J software (NIH, Bethesda). The imaging analyses protocol [14] was able to quantify the muscle fiber orientation distribution from -90 degrees to 90 degrees.

2.2.2. Light sheet microscopy

Light sheet microscopy is a novel fluorescence microscopy technique that applies a planar sheet of light through a transparent sample. The detection lens is set perpendicularly to the light sheet, and the sample is imaged through the light sheet to quickly generate 3D images of a thick tissue or organs with high resolution and anatomic accuracy. The light is emitted and creates a 2D plane or sheet of light across the sample (**Figure 2.7**). The illumination objective that is emitting the light is perpendicular to the tube lens that is collecting the image. The tube lens collects multiples of images of the sample as the sample is rotated.

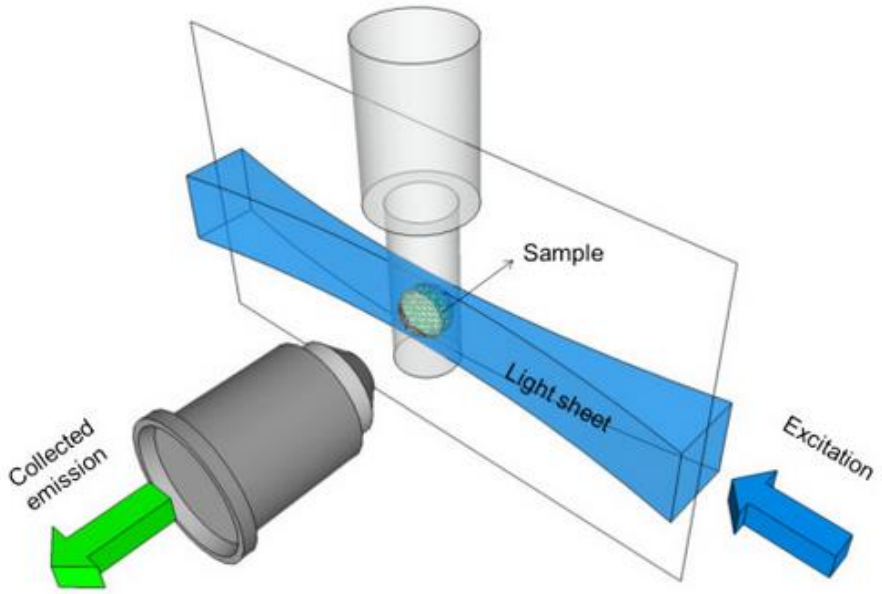

Figure 2.7: Schematic of light sheet microscopy [33].

The novelty of the 2D sheet of light creates a more focused imaging modality than other means of light imaging previously studied. The thinnest region of the light sheet is swept across the entire sample, allowing for uniform illumination and optical sectioning across the whole field of view[33-35]. The high-resolution optical sectioning make 3D rendering of a large volume feasible.

2.3 Tissue clearance, light sheet imaging, and 3D reconstruction and analysis.

2.3.1 Tissue decellularization and tissue clearance

To focus on structural ECM imaging, we performed decellularization on the neonatal and adult LV tissues before tissue clearance, which was required to be conducted prior to light sheet imaging. The tissue samples were ~4 mm in length and ~3 mm in width. The sample thickness

was ~1 mm to allow for imaging. Once the samples were dissected, we mounted the samples via a pin-plastic frame method to prevent tissue shrinkage due to the removal of a large amount of cellular contents (**Figure 2.8**).

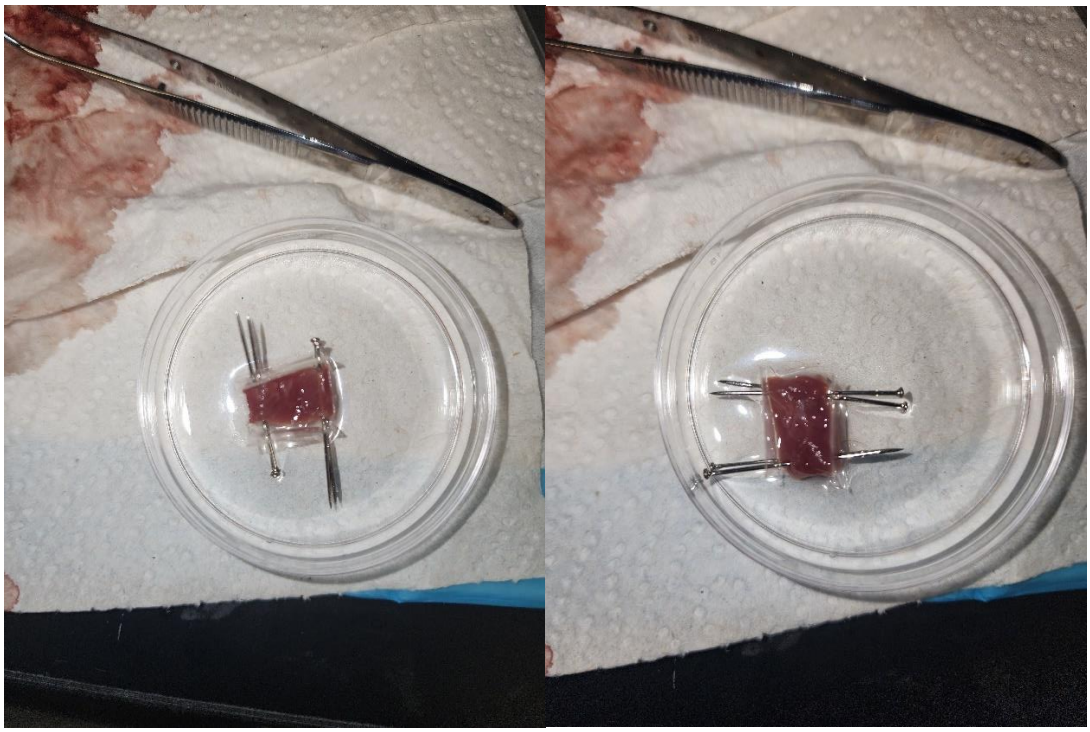

Figure 2.8: Prepared LV samples with a pin-frame mount for tissue decellularization.

The tissue decellularization process involves shaking the samples in a decellularization solution made of 4% SDS in DI water. The samples are shaken continuously for approximately 3 days while changing the media once a day. This allows for the cells to continuously rinsed away from the tissue. The tissue changes from the natural red pigment of the heart to white color (**Figure 2.9**). The white color indicates that there are no more cells within the tissue and the only thing left is the ECM. The acellular neonatal and adult LV samples were then subjected to tissue clearance treatment.

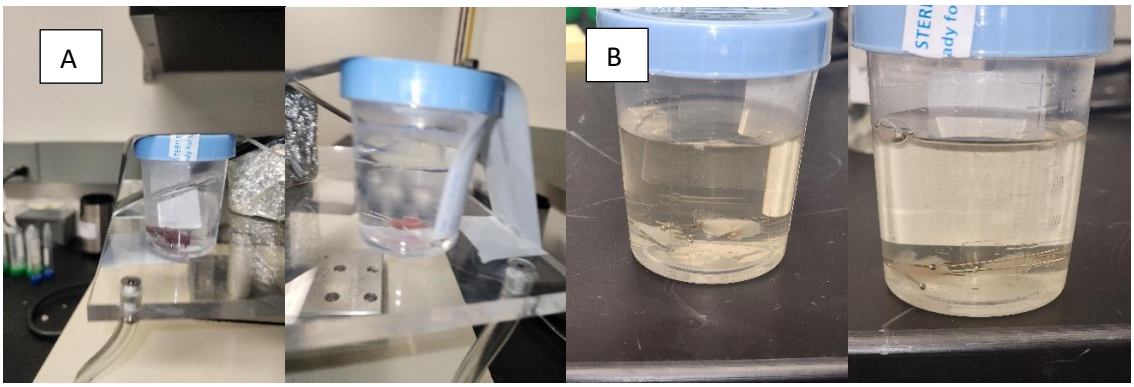

Figure 2.9: Decellularization process. (A) Day 1 of the LV tissues in the SDS solution; (B) Day 3 of the acellular LV tissues in the SDS solution.

Tissue clearance protocol consisted of treating the samples with dehydration 1, rehydration, solution 1 treatment, dehydration 2, and fixation. This was accomplished by creating a media of methanol (20%) to DI water (80%) for dehydration 1. This was sustained at room temperature for one hour. After the hour, the media was changed once an hour increasing the methanol concentration (40%, 60%, 80%, 100% methanol). After the 100% methanol cycle, the methanol was replaced with fresh methanol and stored in the 4 °C refrigerator for 10 minutes. The samples were shaken in a media of dichloromethane/methanol (66%/33%) overnight. The next day, the samples were dehydrated in pure methanol and the media was changed every 30 minutes. The methanol was replaced and stored in the 4 °C refrigerator for 10 minutes. After that, the media was replaced with peroxide/methanol (5%/95%) and stored overnight in the 4 °C refrigerator. The next day, the samples were rehydrated in increments of methanol to DI water (100%methanol, 80%/20%, 60%/40%, 40%/60%, 20%/80%, to 100% DI water). Afterward, the samples were washed in PBS for 1 hour.

The samples were then placed in a media of Solution 1. Solution 1 was a stock made from DI water, PBS, and Trition X-100 (900mL, 100mL, 2mL). This was conducted twice in one-hour increments replacing the media every hour. The samples were then covered in an agarose mixture to fixate a gel around the samples. This was important to allow for imaging with the light sheet microscope. The samples were left to dry overnight in the fume hood. The next day, the excess agarose was trimmed away, and the samples were placed back in their respective vials. After this, dehydration 2 was conducted. The process was started containing a media of methanol to DI water similar to dehydration 1 (20%/80%, 40%/60%, 60%/40%, 80%/20%, 100% methanol) (**Figure 2.10**). The last 100% methanol media change was left overnight. The next day the samples were placed in a 3-hour media of DCM/methanol (66%/33%). The samples were then rinsed thoroughly twice in PBS before placing them in the clearance media of Dibenzyl ether (DBE) for one week. After one week treatment in the DBE media, they were transported to the testing facility for light sheet imaging.

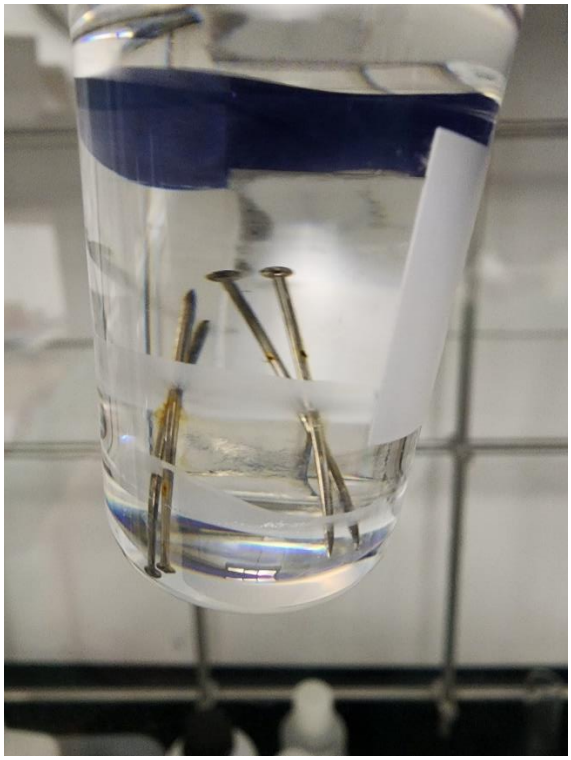

Figure 2.10: Dehydration 2 of the tissue clearance process.

2.3.2 Light sheet imaging

Removed from the DBE media, the sample was laid on a glass petri dish and inspected to ensure that there were no breaks in the sample. To prepare the sample for the light sheet microscopy, three out of the four pins were removed along with the plastic stability sheets. This allowed us to use the remaining pin to be held by the sample holder on the microscope. When the sample was ready it was lowered into the glass chamber filled with DBE. This kept the sample from drying out and allowed for imaging through the light sheet.

The laser from the light sheet microscope emitted a wavelength of light equal to 532 nm **(Figure 2.11A)**. This laser was passed through an aperture. The beam of light exiting the

aperture was then passed through a beam expander. This allowed the diameter of the laser beam to be expanded **(Figure 2.11C)**. The expanded beam of light was then passed through a series of apertures until reached a specific light aperture. This aperture allowed the control of shape of the beam that pass through the sample[37-38]. The microscope collects an image in the form of a 2D sheet. The sample can be shifted from left to right to obtain images of the entirety of the sample. Once the full thickness imaging is complete, the 2D files are collected in the form of a .tif file.

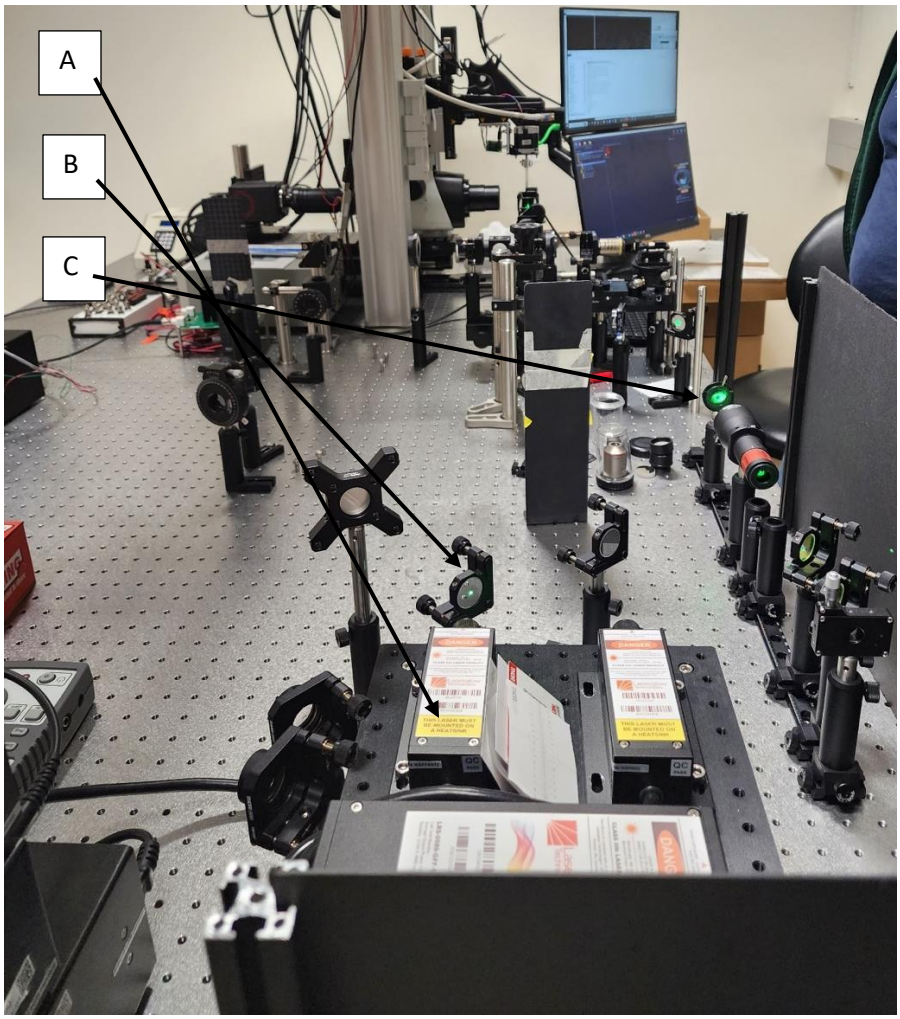

Figure 2.11: Light sheet microscope (Dr. Y. Ding, UTD). (A) 532 nm laser, (B) Angled aperture for redirection of laser, and (C) Beam expander for increased laser diameter.

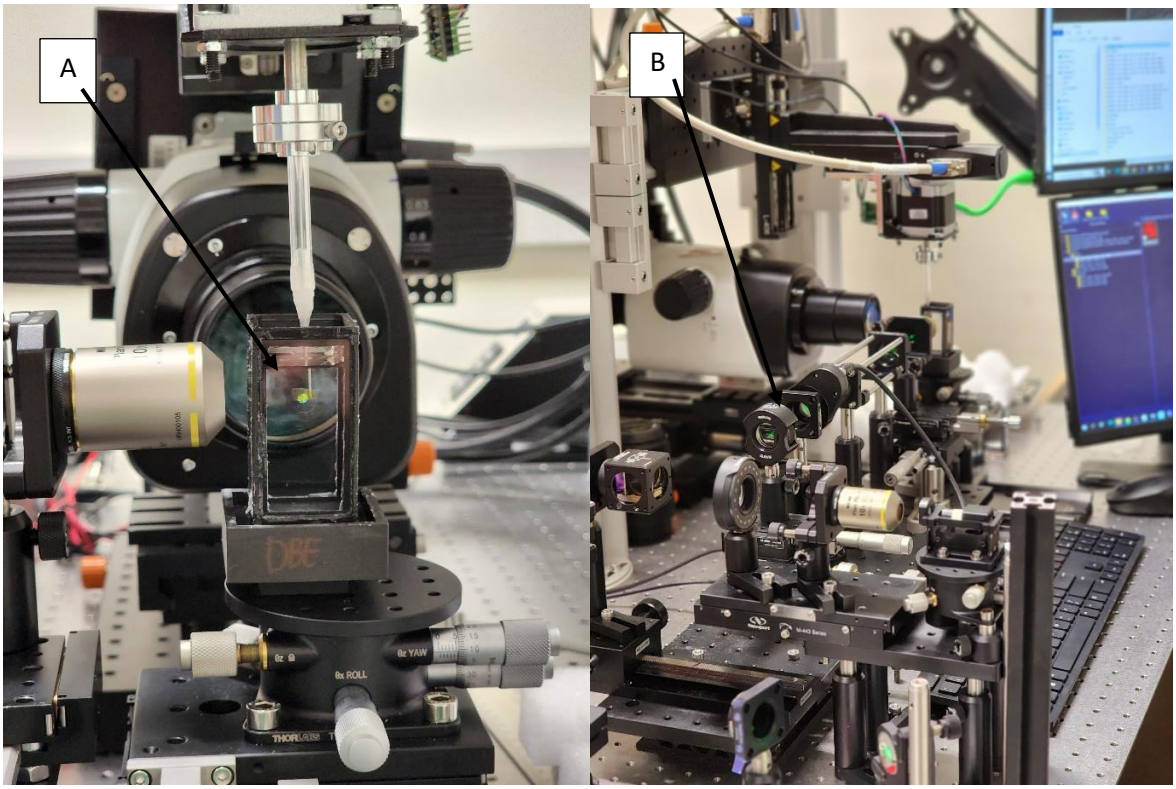

Figure 2.12: Light sheet microscope (Dr. Y. Ding, UTD). (A) Sample tank filled with DBE, (B) Tunable aperture for beam shape that reaches sample.

2.3.3 3D reconstruction and imaging analysis

3D reconstruction of the light sheet images was conducted via Imaris reconstruction software (OXFORD Instruments) **(Figure 2.13)**. This software has a built-in converter to take files that aren't in .tif form and convert them as needed. After loading the light sheet image data, a preliminary 3D rendering was generated. By adjusting the thresholding, the microstructural features could be rendered. For visualization, various shading methods (blend, maximum

intensity projection, or normal shading) could be chosen to produce the needed details. Clipping and sectioning functions could be applied. The clipping allows for multi-directional clipping of the sample that gives the user options for removing artifacts. The section view allows to further adjust the trim threshold by removing sections.

The software allows to analyze the rendering in different magnifications from 1000 um to 100 um[36]. When adjusting the magnification to desired specifications, re-adjusting the threshold and shading parameters was needed to attain the same level of clarification of the sample. It is beneficial in some cases to slice the sample into a reduced section. Slicing could be accomplished from the X, Y, and Z directions. The morphology showed how the fibers of the tissue lay from a top and bottom view. It also showed the depth of layers. For this study, we chose red as the primary rendering color. This made it easier to visualize the morphology of the tissue fibers, and the shading showed higher degrees of detail.

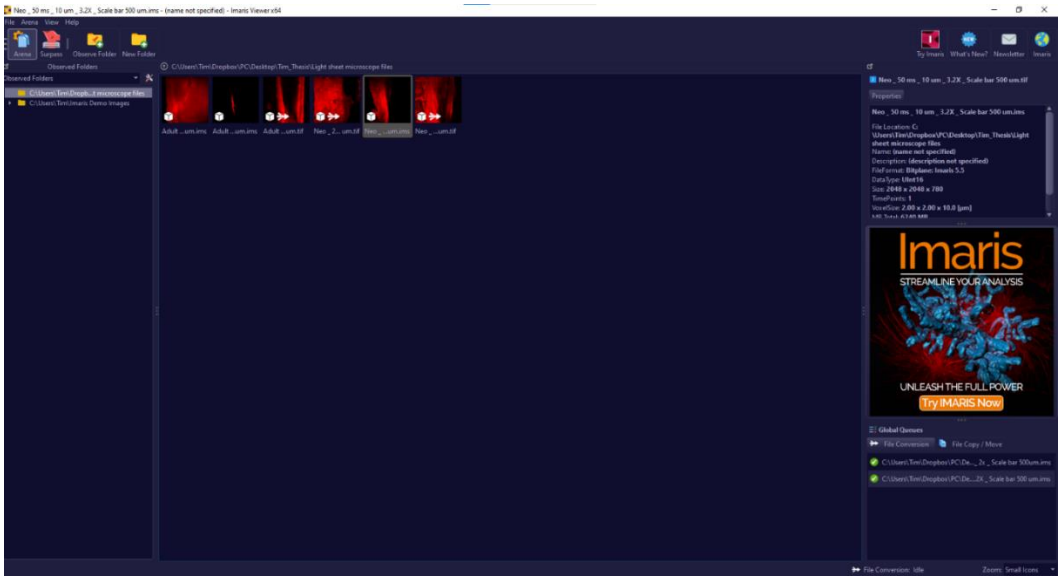

Figure 2.13: Imaris software home screen.

Chapter 3: Results and discussion

3.1 Rheological testing results

Rheological testing results were analyzed after a successful frequency sweep of all samples. The focused sweep frequency of our samples was from 0.1-160 rad/s. This range of frequency was studied due to its covering of physiologically-allowed heartbeat. The rheological testing of the heart muscle tissues generated tissue's elastic modulus (G') and loss modulus (G"), as well as at what frequencies tissues act more elastically or viscously. In theory, both G' and G" contribute to the complex modulus (G*) or the materials resistance to deformation. In the range of frequency sweep (0.1-160 rad/s), we found that overall the adult LV muscle tissues had greater storage modulus than the neonatal LV muscle tissues (**Figure 3.1A,B**). The loss modulus of the adult LV muscle tissues was also overall greater than the neonatal LV tissues (**Figure 3.1C,D**).

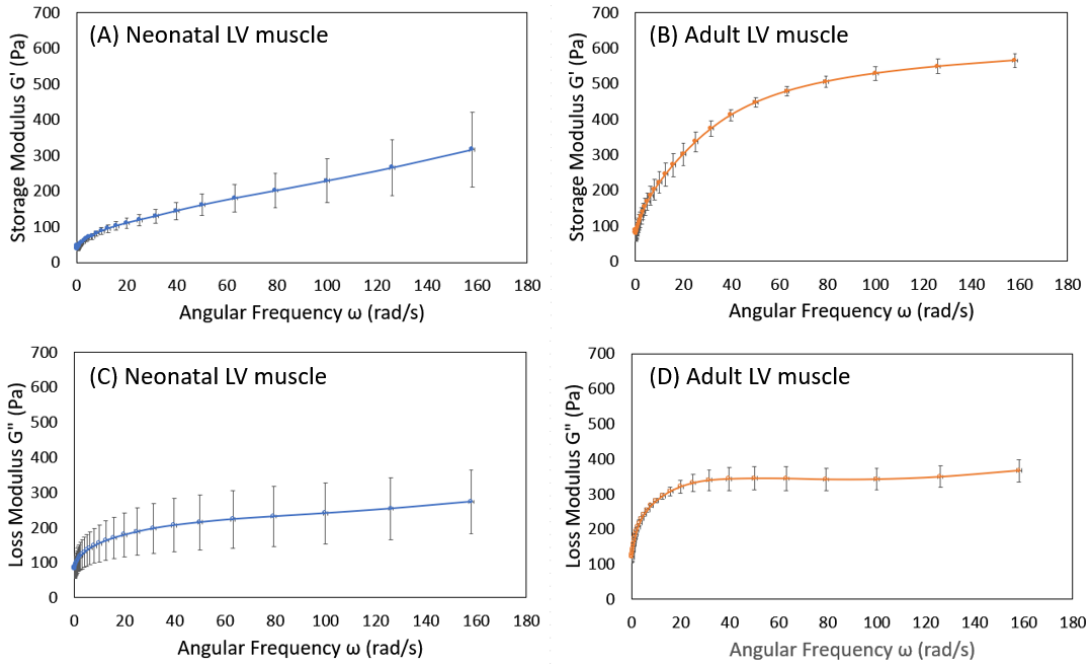

Figure 3.1: (A) Storage modulus of the neonatal LV muscle tissues. (B) Storage modulus of the adult LV muscle tissues. (C) Loss modulus of the neonatal LV muscle tissues. (D) Loss modulus of the adult LV muscle tissues.

We further compared the storage modulus and loss modules at 1 Hz, 2 Hz, 3 Hz, and 10 Hz (Table 1), with the first three frequencies were physiologically relevant and corresponded to heart rates at 60 bpm, 120 bpm and 180 bpm. The first frequency of 1Hz (60 bpm) is a normal heart rate, and most people have an average heart rate around this value. The second frequency of 2 Hz (120 bpm) would be an average heart rate for someone exercising. The third frequency of 3 Hz (180 bpm) is a very high heart rate. Higher than 3 Hz (180 bpm) generally indicates that the person is experiencing supraventricular tachycardia, and the person might experience chest pain or dizziness.

		Neonatal LV muscle (Pa)	Adult LV muscle (Pa)	Ratio of Adult/Neonatal
1 Hz	**Storage Modulus**	75.33 ± 7.08	183.75 ± 26.51	2.44
(6.28 rad/s)	**Loss Modulus**	141.10 ± 47.07	254.44 ± 5.08	1.80
2 Hz	**Storage Modulus**	94.32 ± 10.48	244.70 ± 32.42	2.59
(12.56 rad/s)	**Loss Modulus**	162.63 ± 55.90	294.36 ± 8.13	1.81
3 Hz	**Storage Modulus**	110.03 ± 13.91	301.76 ± 31.47	2.74
(18.84 rad/s)	**Loss Modulus**	178.95 ± 63.08	320.84 ± 17.82	1.79
10 Hz	**Storage Modulus**	179.51 ± 37.85	478.21 ± 14.02	2.66
(62.83 rad/s)	**Loss Modulus**	223.51 ± 82.60	344.13 ± 33.47	1.54

Table 1: Storage modulus and loss modulus of the neonatal LV muscle tissues and adult LV muscle tissues at 1 Hz, 2 Hz, 3 Hz, and 10 Hz.

At the examined frequencies (1 Hz, 2 Hz, 3 Hz, and 10 Hz), the storage moduli were ~2.5 times larger than the nonanal LV muscle tissues, and the loss modulus were ~1.8 times larger than the nonanal LV muscle tissues (**Table 1**). We also noticed that G' of the neonatal LV muscle tissues had a relative linear increasing trend in the frequency range of 10-80 rad/s, while the increase trend for the adult LV muscle tissues had an obvious nonlinear trend.

3.2 Histological images and orientation analysis.

While the heart muscle fibers in the adult LV exhibited aligned and tight packing muscle fiber and distinguishing muscle bundle morphology (**Figure 3.3**), the heart muscle fibers in neonatal LV showed muscle fibers had a loose packing, less aligned, and more locally wavy morphology (**Figure 3.2**). The histological images also showed that minimum collagen content (yellow color) exist in the neonatal LV and more proteoglycans (blue) associate with the immature heart muscle fibers (**Figure 3.2**). On the other hand, much more collagen fiber stain (yellow color) was observed in the adult LV histological images, and the amount of proteoglycans (blue color) was also found to decrease (**Figure 3.3**) when compared with the neonatal LV. This can be further

examined in the 10X magnification of the histological study **(Figure 3.4)**. Heart muscle fiber orientation distributions were quantified from histological images of neonatal LV circumferential section, neonatal LV longitudinal section, and adult LV circumferential section, and adult LV longitudinal section. Consistent with the visual observation, the qualified results demonstrated that the neonatal LV muscles showed less aligned muscle fiber orientation when compared to the adult LV muscle fiber orientation (**Figure 3.5A-D**). The muscle fiber alignment in the adult LV longitudinal section (**Figure 3.5D**) was higher than the adult LV circumferential section (**Figure 3.5C**). However, the muscle fiber alignment in the neonatal LV longitudinal section (**Figure 3.5B**) was lower than the neonatal LV circumferential section (**Figure 3.5A**).

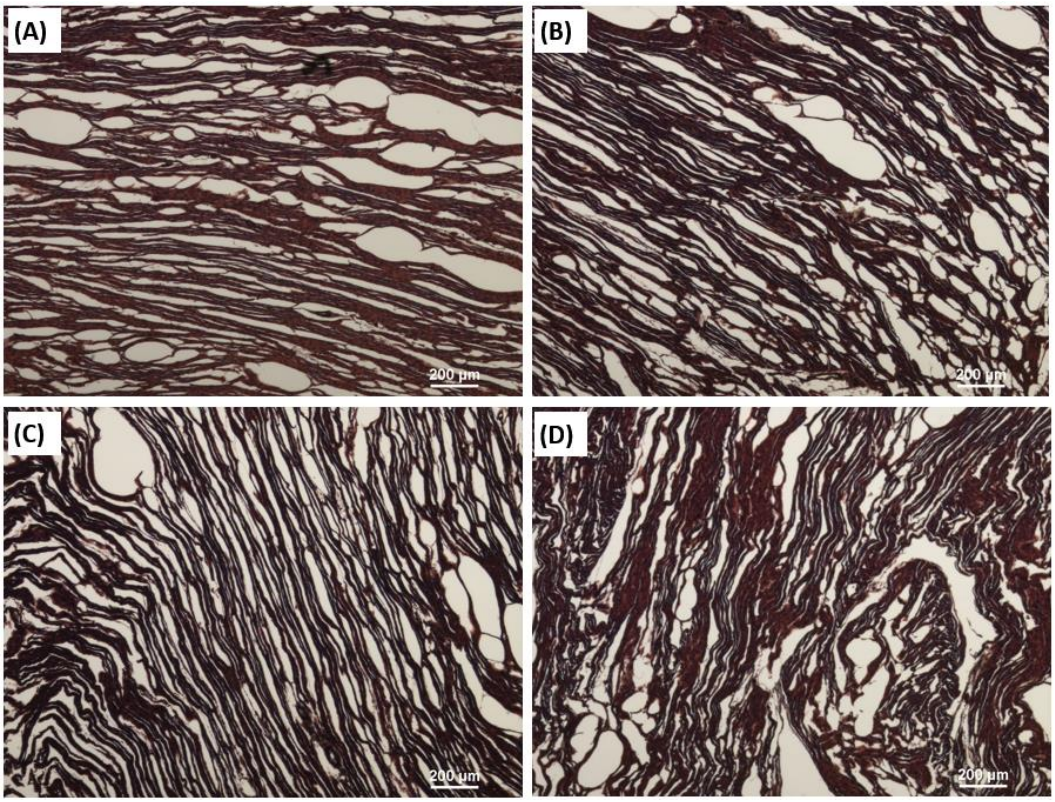

Figure 3.2: Movat's pentachrome staining for (A) and (B) Neonatal LV circumferential sections; (C) and (D) Neonatal LV longitudinal sections. Heart muscle: red, collagen: yellow, Proteoglycans: blue, Elastin: black.

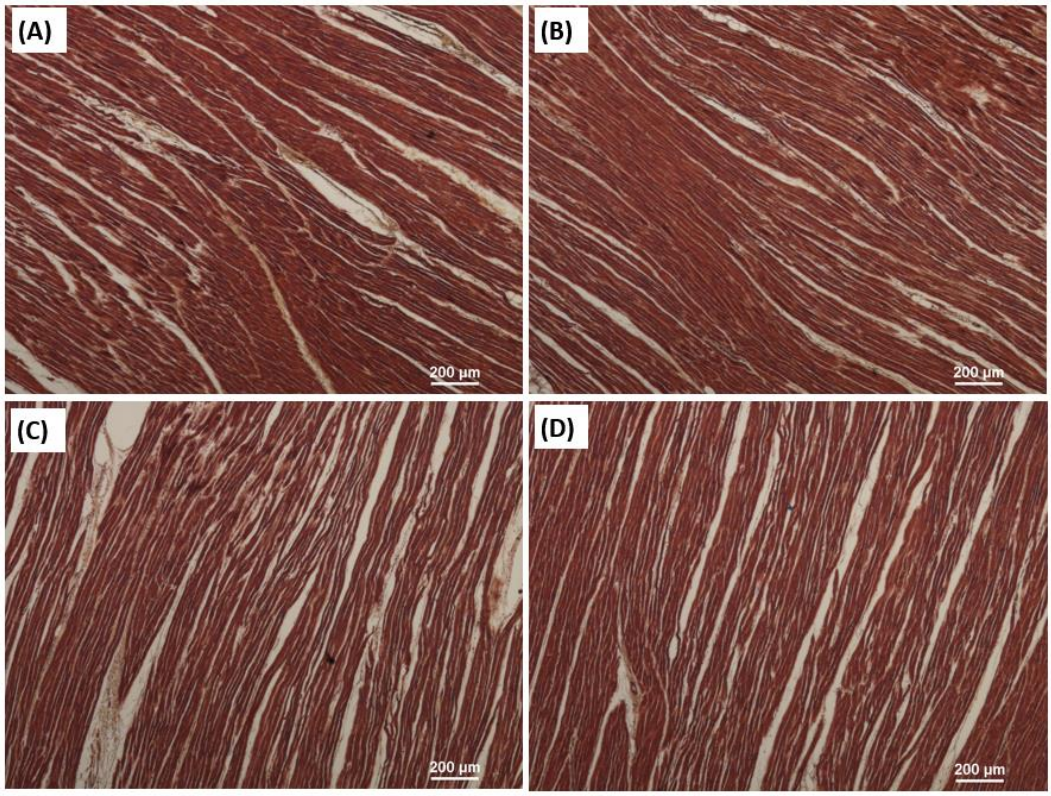

Figure 3.3: Movat's pentachrome staining at 4X magnification for (A) and (B) Adult LV circumferential sections; (C) and (D) Adult LV longitudinal sections. Heart muscle: red, collagen: yellow, Proteoglycans: blue, Elastin: black.

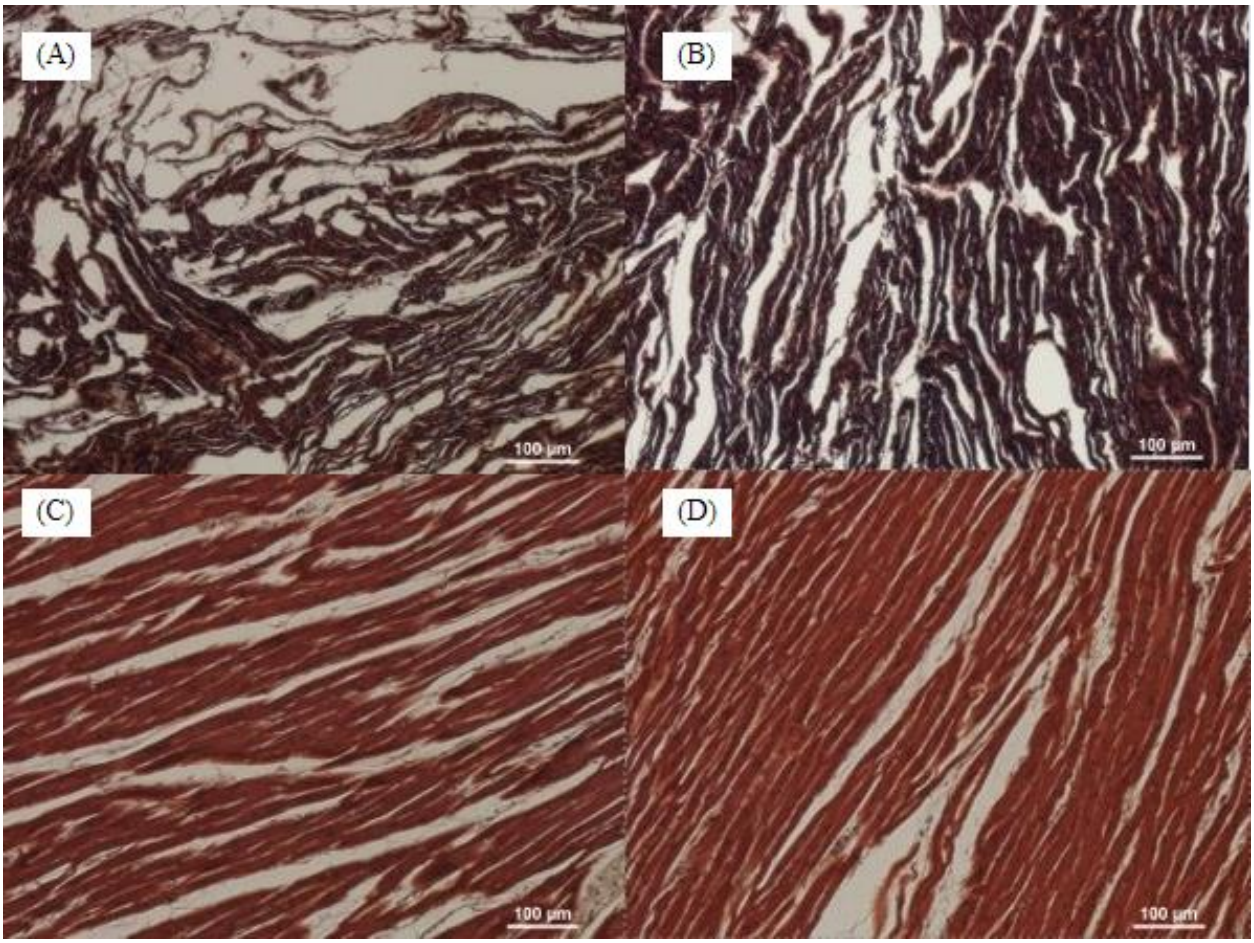

Figure 3.4: Movat's pentachrome staining at 10X magnification for (A) Neonatal LV circumferential section; (B) Neonatal LV longitudinal section; (C) Adult LV circumferential section; (D) Adult LV longitudinal section. Heart muscle: red, collagen: yellow, Proteoglycans: blue, Elastin: black.

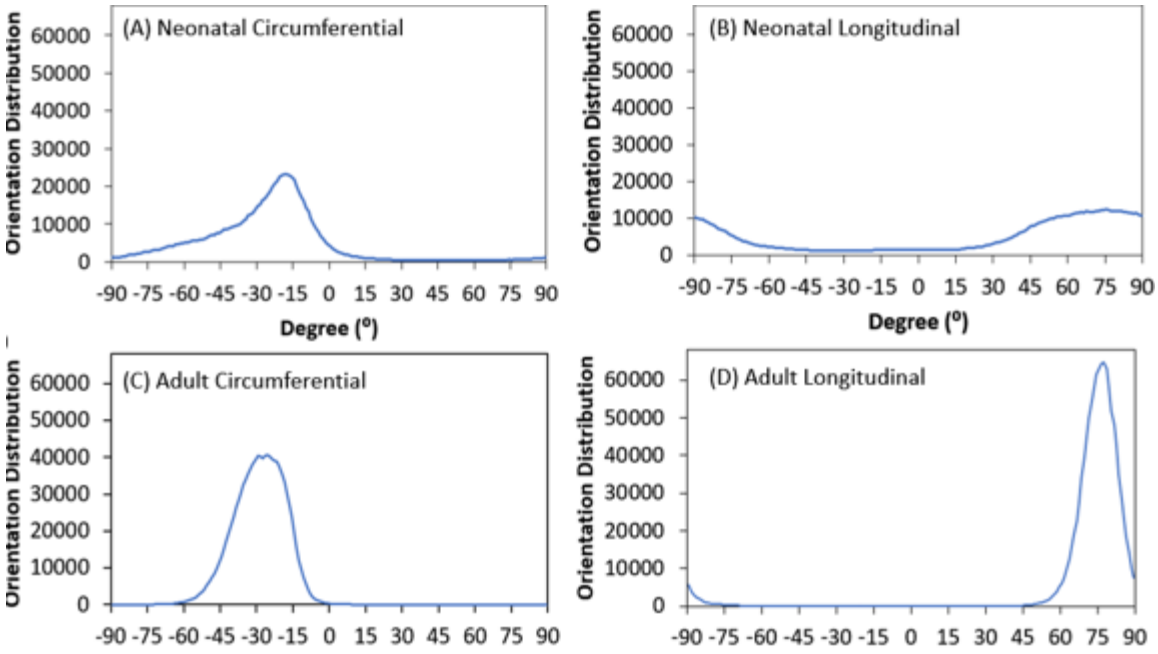

Figure 3.5: Heart muscle fiber orientation distribution for (A) Neonatal LV circumferential section, (B) Neonatal LV longitudinal section, (C) Adult LV circumferential section, and (D) Adult LV longitudinal section.

3.3 Light sheet imaging results

3D reconstruction began with the light sheet images being loaded into the workspace window **(Figure 3.6)**. In the workspace window, rendering starts at 1000 µm. Image thresholding helps to capture the fiber signals and achieve detailed 3D structure from rendering. The clipping tool in the top left of the work window is indicated by a small pair of scissors. Clipping allows to focus on the region of interest to study the details of fiber morphology (**Figure 3.7**). After thresholding segmentation and 3D rendering, we were able to reconstruct 3D light sheet images of the acellular neonatal LV ECM and the acellular neonatal LV ECM (**Figure 3.8**). Both the acellular neonatal LV ECM and the acellular neonatal LV ECM showed the ECM network, primarily collagen fibers, with neonatal LV ECM exhibiting less denser morphology when compared with adult LV ECM (**Figure 3.8**).

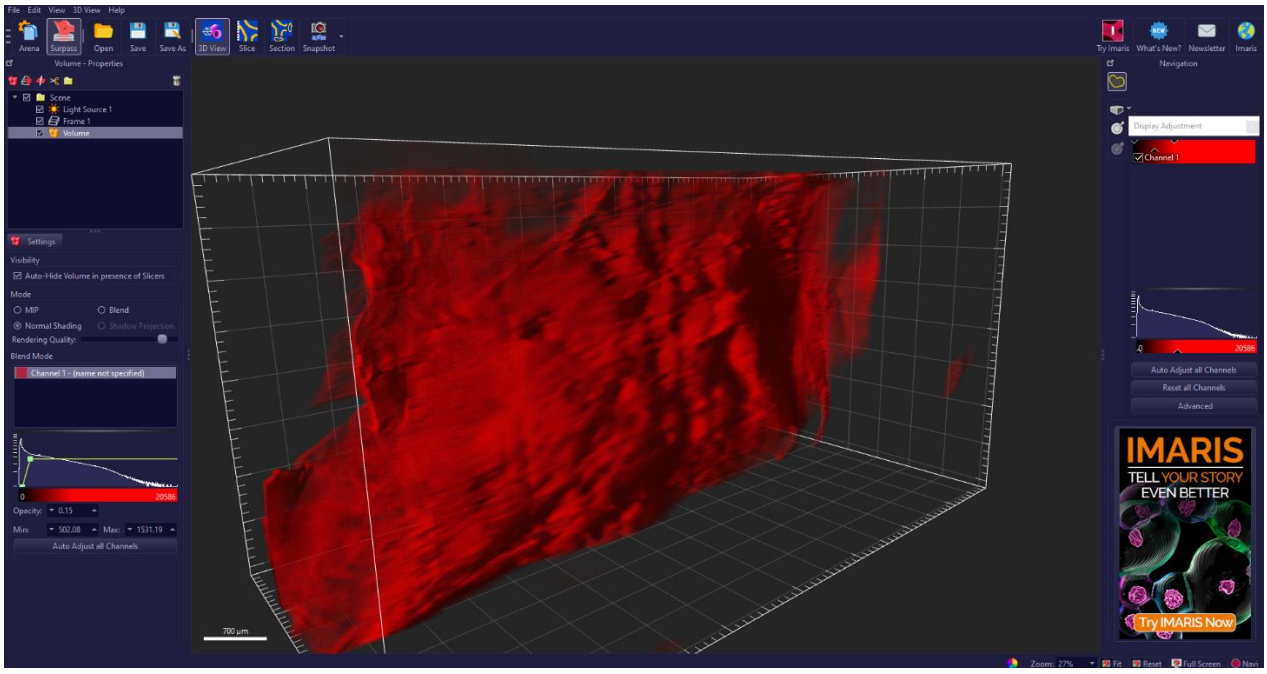

Figure 3.6: Initial rendering of sample in the workspace window.

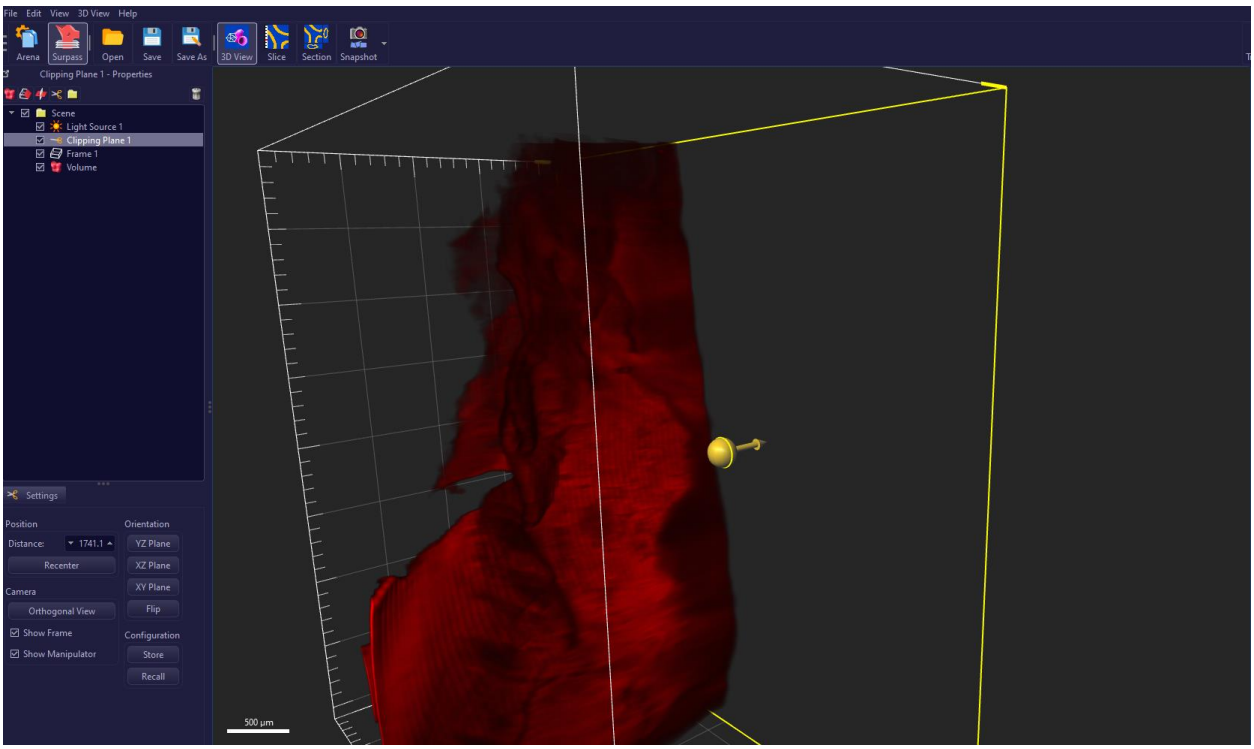

Figure 3.7: Clipping of sample in Imaris.

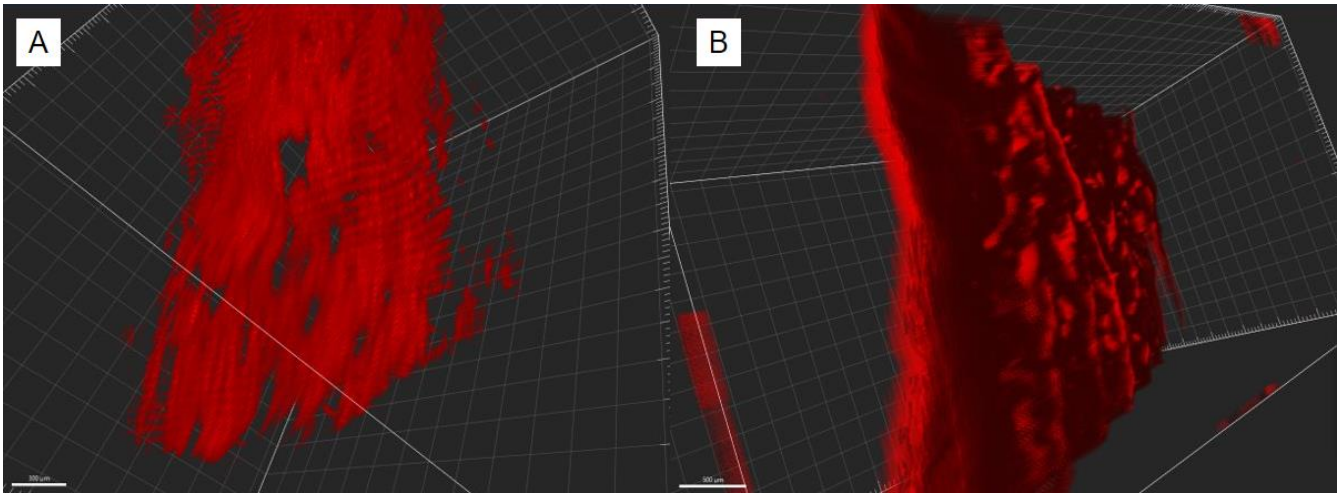

Figure 3.8: 3D light sheet images of (A) the acellular neonatal LV ECM and (B) the acellular adult LV ECM.

3.4 Conclusions, Discussions, and Future Studies

In conclusion, we found that the dynamic viscoelastic properties of the neonatal porcine LV muscle tissues were drastically different from the adult LV muscle tissues. The adult LV muscle tissues had much greater storage modulus (G') and larger loss modulus (G") than the neonatal LV muscle tissues in the range of frequency sweep. The difference in G' between neonatal and adult echoes with the passive mechanical properties observed in tensile testing [40]. We speculate that, in the neonatal LV tissue the collagen network that binds the heart muscle fibers is still immature and will experience rapid deposition and maturation during the later developmental stages. This could be one of factors that resulted in the unique dynamic viscoelastic behavior of the neonatal heart muscles.

Our histological observation not only verified the speculation on the role of immature collagen network in affecting dynamic viscoelastic properties of neonatal LV tissues, but also

revealed more factors that might contribute the observed differences in biomechanical properties [41-42]. Another important observation is the cardiomyocytes in the neonatal LV tissues were much more immature than the heart muscle fibers of the adult LV both in cellular phenotype and cellular microstructural organization. The heart muscle fibers in neonatal LV showed muscle fiber had a loose packing, less aligned, and more locally wavy morphology, while the heart muscle fibers in the adult LV exhibited aligned and tight packing muscle fiber and distinguishing muscle bundle morphology [43-46]. The histological images also showed that more proteoglycans (blue staining) were associated with the immature heart muscle fibers. When compared with the adult LV tissues, all those cellular, ECM, and microstructural differences in the neonatal LV tissues might contribute to the observed differences in dynamic viscoelastic properties.

Lastly, we have developed a tissue preparation and imaging protocol that was able to capture 3D ECM fiber orientation and alignment for both the neonatal and adult heart muscles. We designed a decellularization procedure before tissue clearance in order to focus on imaging only the 3D ECM structure by removing the cellular content physically [47-50]. The pin-frame method was used with an intention to prevent ECM scaffold collapse after decellularization. We found that the pin-frame method was able to prevent collapse along length and width of the mounted sample but failed to prevent the collapse along the thickness. This pitfall was the reason why we visualized a dense ECM network, primarily collagen fibers, in both the acellular neonatal LV and adult LV tissues. Future study will use the native tissues of neonatal LV and adult LV, and subject the samples directly to tissue clearance. With the cellular content being preserved, the light sheet imaging will capture both the heart muscle fibers and the ECM network. If the autofluorescence of heart muscle fibers and the autofluorescence of the ECM

network overlap to each other, we will identify specific fluorescent staining for collagen network, so as to distinguish the collagen morphology from the heart muscle fibers.

REFERENCES

1. Ahmad, F. B., Cisewski, J. A., Xu, J., & Anderson, R. N. (2023). Provisional Mortality Data — United States, 2022. *Morbidity and Mortality Weekly Report*, *72*(18), 488–492. https://doi.org/10.15585/mmwr.mm7218a3

2. *Health and Economic Costs of Chronic Diseases | CDC*. (n.d.). https://www.cdc.gov/chronicdisease/about/costs/index.htm

3. *Heart disease - Symptoms and causes - Mayo Clinic*. (2022, August 25). Mayo Clinic. https://www.mayoclinic.org/diseases-conditions/heart-disease/symptoms-causes/syc-20353118

4. Olvera Lopez E, Ballard BD, Jan A. Cardiovascular Disease. [Updated 2022 Aug 8]. In: StatPearls [Internet]. Treasure Island (FL): StatPearls Publishing; 2023 Jan-. Available from: https://www.ncbi.nlm.nih.gov/books/NBK535419/

5. W. Raab, "The Nonvascular Metabolic Myocardial Vulnerability Factor in "Coronary Heart Disease": Fundamentals of Pathogenesis, Treatment, and Prevention," Am HeartJ, vol. 66, pp. 685-706, 1963.

6. G. Baroldi, "Acute coronary occlusion as a cause of myocardial infarct and sudden coronary heart death," Am J Cardiol, vol. 16, no. 6, pp. 859-880, 1965.

7. G. Baroldi, "Coronary heart disease: significance of the morphologic lesions," Am HeartJ vol. 85, pp. 1-5, 1973.

8. F. Shaffer, R. McCraty, and C. L. Zerr, "A healthy heart is not a metronome: an integrative review of the heart's anatomy and heart rate variability," (in eng), Front Psychol, vol. 5, p. 1040, 2014, doi: 10.3389/fpsyg.2014.01040.

9. W. C. Stanley, F. A. Recchia, and G. D. Lopaschuk, "Myocardial substrate metabolismin the normal and failing heart," (in eng), Physiol Rev, vol. 85, no. 3, pp. 1093-129, Jul2005, doi: 10.1152/physrev.00006.2004.

10. Elite Cardiovascular Group. (2020, November 4). *Myocardial Infarction (Heart Attack) - Elite Cardiovascular Group*.

https://www.elitecardiovascular.com/cardiovascular-conditions/cardiac-conditions/myocardial-infarctions-heart-attacks/

11. Reddy K, Khaliq A, Henning RJ. Recent advances in the diagnosis and treatment of acute myocardial infarction. World J Cardiol. 2015 May 26;7(5):243-76. doi: 10.4330/wjc.v7.i5.243. PMID: 26015857; PMCID: PMC4438466.

12. Shirotani, M., Togi, K., & Ohi, Y. (2014). Current Problems in the Treatment of Acute Myocardial Infarction: For Better Reperfusion and Long-Term Benefits. *Emergency Medicine*, *04*(06). https://doi.org/10.4172/2165-7548.1000220

13. Zhu, W., Zhang, E. E., Zhao, M., Chong, Z., Fan, C., Tang, Y., Hunter, J. D., Borovjagin, A. V., Walcott, G. P., Chen, J. Y., Qin, G., & Zhang, J. (2018). Regenerative Potential of Neonatal Porcine Hearts. *Circulation*, *138*(24), 2809–2816. https://doi.org/10.1161/circulationaha.118.034886

14. Velayutham N, Yutzey KE. Porcine Models of Heart Regeneration. J Cardiovasc Dev Dis. 2022 Mar 23;9(4):93. doi: 10.3390/jcdd9040093. PMID: 35448069; PMCID: PMC9025077.

15. Ahmad, F., Prabhu, R., Liao, J., Soe, S., Jones, M. P., Miller, J., Berthelson, P. R., Enge, D., Copeland, K. M., Shaabeth, S. A., Johnston, R. C., Maconochie, I., & Theobald, P. (2018). Biomechanical properties and microstructure of neonatal porcine ventricles. *Journal of the Mechanical Behavior of Biomedical Materials*, *88*, 18–28. https://doi.org/10.1016/j.jmbbm.2018.07.038

16. A. B. Aurora et al., "Macrophages are required for neonatal heart regeneration," (in eng), J Clin Invest, vol. 124, no. 3, pp. 1382-92, Mar 2014, doi: 10.1172/jci72181.

17. E. R. Porrello et al., "Transient regenerative potential of the neonatal mouse heart," (ineng), Science, vol. 331, no. 6020, pp. 1078-80, Feb 25 2011, doi: 10.1126/science.1200708.

18. M. Günthel, P. Barnett, and V. M. Christoffels, "Development, Proliferation, and Growthof the Mammalian Heart," (in eng), Mol Ther, vol. 26, no. 7, pp. 1599-1609, Jul 5 2018,doi: 10.1016/j.ymthe.2018.05.022.

19. M. Isomi, T. Sadahiro, and M. Ieda, "Progress and Challenge of Cardiac Regenerationto Treat Heart Failure," (in eng), J Cardiol, vol. 73, no. 2, pp. 97-101, Feb 2019, doi:10.1016/j.jjcc.2018.10.002.

20. K. D. Poss, L. G. Wilson, and M. T. Keating, "Heart regeneration in zebrafish," (in eng),Science, vol. 298, no. 5601, pp. 2188-90, Dec 13 2002, doi: 10.1126/science.1077857.

21. Z. Wang et al., "Mechanistic basis of neonatal heart regeneration revealed by transcriptome and histone modification profiling," (in eng), Proc Natl Acad Sci U S A,vol. 116, no. 37, pp. 18455-18465, Sep 10 2019, doi: 10.1073/pnas.1905824116.

22. M. Xin, E. N. Olson, and R. Bassel-Duby, "Mending broken hearts: cardiac development as a basis for adult heart regeneration and repair," (in eng), Nat Rev Mol Cell Biol, vol.14, no. 8, pp. 529-41, Aug 2013, doi: 10.1038/nrm3619.

23. S. A. Jesty et al., "c-kit+ precursors support postinfarction myogenesis in the neonatal,but not adult, heart," (in eng), Proc Natl Acad Sci U S A, vol. 109, no. 33,pp. 13380-5,Aug 14 2012, doi: 10.1073/pnas.1208114109.

24. C. Jopling, E. Sleep, M. Raya, M. Martí, A. Raya, and J. C. Izpisúa Belmonte, "Zebrafishheart regeneration occurs by cardiomyocyte dedifferentiation and proliferation," (in eng),Nature, vol. 464, no. 7288, pp. 606-9, Mar 25 2010, doi: 10.1038/nature08899.

25. Copeland, K. M., Brazile, B., Butler, J. N., Cooley, J., Brinkman-Ferguson, E. L., Claude, A., Lin, S., Rais-Rohani, S., Welch, B. A., McMahan, S. R., Nguyen, K. T., Hong, Y., Ramaswamy, S., Liu, Z., Bajona, P., Peltz, M., & Liao, J. (2022). Investigating the Transient Regenerative Potential of Cardiac Muscle Using a Neonatal Pig Partial Apical Resection Model. *Bioengineering*, *9*(8), 401. https://doi.org/10.3390/bioengineering9080401

26. Wang, B.; Tedder, M.E.; Perez, C.E.; Wang, G.; Curry, A.L.D.J.; To, F.; Elder, S.H.; Williams, L.N.; Simionescu, D.T.; Liao, J. Structural and biomechanical characterizations of porcine myocardial extracellular matrix. J. Mater. Sci. Mater. Med. **2012**, 23, 1835–1847.

27. Wang, B.; Williams, L.N.; Curry, A.L.D.J.; Liao, J. Preparation of acellular myocardial scaffolds with well-preserved cardiomyocyte lacunae, and method for applying mechanical and electrical simulation to tissue construct. In Cardiac Tissue Engineering; Humana Press: New York, NY, USA, 2014; Volume 1181, pp. 189–202.

28. Zhang, S.; Crow, J.A.; Yang, X.; Chen, J.; Borazjani, A.; Mullins, K.B.; Chen, W.; Cooper, R.C.; McLaughlin, R.M.; Liao, J. The Correlation of 3D DT-MRI Fiber

Disruption with Structural and Mechanical Degeneration in Porcine Myocardium. Ann. Biomed. Eng. **2010**, 38, 3084–3095.

29. Ahmad F, Soe S, White N, Johnston R, Khan I, Liao J, Jones M, Prabhu R, Maconochie I, Theobald P. Region-Specific Microstructure in the Neonatal Ventricles of a Porcine Model. Ann Biomed Eng. 2018 Dec;46(12):2162-2176. doi: 10.1007/s10439-018-2089-4. Epub 2018 Jul 16. PMID: 30014287; PMCID: PMC6267669.

30. Anton Paar MCR Series instruction manual, MCR 52/MCR 102/ MCR 302, EC-Twist 302/EC-Twist 502

31. Anton Paar RheoCompass™ Software, software manual

32. Wright GJ, Brockbank KG, Rahn E, Halwani DO, Chen Z, Yao H. Impact of storage solution formulation during refrigerated storage upon chondrocyte viability and cartilage matrix. Cells Tissues Organs. 2014;199(1):51-8. doi: 10.1159/000363134. Epub 2014 Aug 21. PMID: 25171188; PMCID: PMC4184947.

33. Omar E. Olarte, Jordi Andilla, Emilio J. Gualda, and Pablo Loza-Alvarez, "Light-sheet microscopy: a tutorial," Adv. Opt. Photon. **10**, 111-179 (2018)

34. Patel, K.B., Liang, W., Casper, M.J. *et al.* High-speed light-sheet microscopy for the in-situ acquisition of volumetric histological images of living tissue. *Nat. Biomed. Eng* **6**, 569–583 (2022). https://doi.org/10.1038/s41551-022-00849-7

35. Chakraborty, T., Driscoll, M.K., Jeffery, E. *et al.* Light-sheet microscopy of cleared tissues with isotropic, subcellular resolution. *Nat Methods* **16**, 1109–1113 (2019). https://doi.org/10.1038/s41592-019-0615-4

36. Fogarty MJ, Hammond LA, Kanjhan R, Bellingham MC, Noakes PG. A method for the three-dimensional reconstruction of Neurobiotin™-filled neurons and the location of their synaptic inputs. Front Neural Circuits. 2013 Oct 1;7:153. doi: 10.3389/fncir.2013.00153. PMID: 24101895; PMCID: PMC3787200.

37. Sodimu O, Almasian M, Gan P, Hassan S, Zhang X, Liu N, Ding Y. Light sheet imaging and interactive analysis of the cardiac structure in neonatal mice. J Biophotonics. 2023 Jan 9:e202200278. doi: 10.1002/jbio.202200278. Epub ahead of print. PMID: 36624523.

38. Ding, Y., Ma, J., Langenbacher, A. D., Baek, K. Y., Lee, J., Chang, C., Hsu, J. J., Kulkarni, R. P., Belperio, J. A., Shi, W., Ranjbarvaziri, S., Ardehali, R., Tintut, Y., Demer, L. L., Chen, J., Fei, P., Packard, R. R. S., & Hsiai, T. K. (2018). Multiscale light-sheet for rapid imaging of cardiopulmonary system. *JCI Insight*, *3*(16). https://doi.org/10.1172/jci.insight.121396

39. Rezakhaniha, R., et al., *Experimental investigation of collagen waviness and orientation in the arterial adventitia using confocal laser scanning microscopy.* Biomechanics and modeling in mechanobiology, 2012. **11**(3-4): p. 461-473.

40. Valeanu L, Ginghina C, Bubenek-Turconi S. Blood Rheology Alterations in Patients with Cardiovascular Diseases. Rom J Anaesth Intensive Care. 2022 Dec 29;28(2):41-46. doi: 10.2478/rjaic-2021-0007. PMID: 36844116; PMCID: PMC9949020.

41. Salvatore L, Gallo N, Natali ML, Terzi A, Sannino A, Madaghiele M. Mimicking the Hierarchical Organization of Natural Collagen: Toward the Development of Ideal Scaffolding Material for Tissue Regeneration. Front Bioeng Biotechnol. 2021 Apr 27;9:644595. doi: 10.3389/fbioe.2021.644595. PMID: 33987173; PMCID: PMC8112590.

42. Shoulders MD, Raines RT. Collagen structure and stability. Annu Rev Biochem. 2009;78:929-58. doi: 10.1146/annurev.biochem.77.032207.120833. PMID: 19344236; PMCID: PMC2846778.

43. Reznikov, N., Shahar, R., & Weiner, S. (2014). Three-dimensional structure of human lamellar bone: The presence of two different materials and new insights into the hierarchical organization. *Bone*, *59*, 93–104. https://doi.org/10.1016/j.bone.2013.10.023

44. Reznikov, N., Almany-Magal, R., Shahar, R., & Weiner, S. (2013). Three-dimensional imaging of collagen fibril organization in rat circumferential lamellar bone using a dual beam electron microscope reveals ordered and disordered sub-lamellar structures. *Bone*, *52*(2), 676–683. https://doi.org/10.1016/j.bone.2012.10.034

45. Petrossian, E., Reddy, V., Collins, K. K., Culbertson, C. B., Macdonald, M., Lamberti, J. J., Reinhartz, O., Mainwaring, R. D., Francis, P. T., Malhotra, S. P., Gremmels, D. B., Suleman, S., & Hanley, F. L. (2006). The extracardiac conduit Fontan operation using minimal approach extracorporeal circulation: Early and midterm outcomes. *The Journal of Thoracic and Cardiovascular Surgery*, *132*(5), 1054–1063. https://doi.org/10.1016/j.jtcvs.2006.05.066

46. Sommer, G., Schriefl, A. J., Andrä, M., Sacherer, M., Viertler, C., Wolinski, H., & Holzapfel, G. (2015). Biomechanical properties and microstructure of human ventricular myocardium. *Acta Biomaterialia*, *24*, 172–192. https://doi.org/10.1016/j.actbio.2015.06.031

47. Richardson, D.S., Guan, W., Matsumoto, K. *et al.* Tissue clearing. *Nat Rev Methods Primers* **1**, 84 (2021). https://doi.org/10.1038/s43586-021-00080-9

48. Richardson, D. S. & Lichtman, J. W. Clarifying tissue clearing. *Cell* **162**, 246–257 (2015).

49. Tainaka, K., Kuno, A., Kubota, S. I., Murakami, T. & Ueda, H. R. Chemical principles in tissue clearing and staining protocols for whole-body cell profiling. *Annu. Rev. Cell Dev. Biol.* **32**, 713–741 (2016).

50. Lee, E. et al. ACT-PRESTO: rapid and consistent tissue clearing and labeling method for 3-dimensional (3D) imaging. *Sci. Rep.* **6**, 18631 (2016).